THE ASTROPHYSICAL JOURNAL, 554:694–709, 2001 June 20

SPECTRA OF THE $\frac{1}{4}$ keV X-RAY DIFFUSE BACKGROUND FROM THE DIFFUSE X-RAY SPECTROMETER EXPERIMENT

W. T. SANDERS, RICHARD J. EDGAR,[1] W. L. KRAUSHAAR, D. MCCAMMON, AND J. P. MORGENTHALER
University of Wisconsin, Madison, Madison, WI, 53706; sanders@dxs.ssec.wisc.edu
Received 2000 May 23; accepted 2001 February 16

ABSTRACT

The Diffuse X-ray Spectrometer (DXS) flew as an attached payload on the STS-54 mission of the space shuttle *Endeavour* in 1993 January and obtained spectra of the soft X-ray diffuse background in the 148–284 eV (84–44 Å) band using a Bragg-crystal spectrometer. The spectra show strong emission lines, indicating that the emission is primarily thermal. Since the observations were made at low Galactic latitude, this thermal emission must arise from a nearby hot component of the interstellar medium, most likely the Local Hot Bubble, a region within $\sim$100 pc of the Sun characterized by an absence of dense neutral gas. The DXS spectrum of the hot interstellar medium is not consistent with either collisional equilibrium models or with nonequilibrium ionization models of the X-ray emission from astrophysical plasmas. Models of X-ray emission processes appear not yet adequate for detailed interpretation of these data. The DXS data are most nearly consistent with models of thermal emission from a plasma with a temperature of $10^{6.1}$ K and depletions of refractory elements magnesium, silicon, and iron to levels $\sim$30% of solar.

Subject headings: ISM: lines and bands — radiation mechanisms: thermal — X-rays: galaxies — X-rays: general — X-rays: ISM

1. INTRODUCTION

The diffuse X-ray background in the $\frac{1}{4}$ keV energy band (roughly 120–284 eV or 100–44 Å) has been studied for over 30 yr since the initial observations by Bowyer, Field, & Mack (1968), Henry et al. (1968), and Bunner et al. (1969). Although great progress has been made in determining the spatial distribution of this emission, knowledge of its spectral characteristics has lagged. An excellent review of the current state of our understanding of the hot phase of the ISM is that of Snowden (2001).

1.1. *Spatial Structure*

The angular distribution of the $\frac{1}{4}$ keV X-ray background over the whole sky has been mapped by a series of sounding rocket flights (the C band; McCammon et al. 1983), by the *SAS 3* satellite (Marshall & Clark 1984), by the *HEAO 1* satellite (Garmire et al. 1992), and by the *ROSAT* satellite (the R12 band; Snowden et al. 1995, 1997). When the counting rates of these four $\frac{1}{4}$ keV maps are compared, allowing for the different instrumental responses, they agree with each other to better than a few percent, except that the *ROSAT* count rates are consistently $\sim$10% lower than expected (Snowden et al. 1995).

Three of the surveys (McCammon et al. 1983; Garmire et al. 1992; Snowden et al. 1995, 1997) produced all-sky maps at higher X-ray energies, greater than 500 eV, that have angular structure similar to one another but very different from that of the $\frac{1}{4}$ keV maps. One of the surveys (McCammon et al. 1983) produced an all-sky map in the lower energy 130–188 eV band (95–66 Å, the B band) that is very similar in appearance to that of the $\frac{1}{4}$ keV surveys. Sounding rocket observations of the diffuse background over $\sim$1.7 sr at even lower energies (Bloch et al. 1986; Juda et al. 1991; Edwards 1990) found that the ratio of intensity in the 70–111 eV band (177–112 Å, the Be band) to that of the B band was essentially constant. These broadband all-sky data suggest a picture in which a soft component provides almost all of the intensity seen in the Be band and B band, most of the intensity in the $\frac{1}{4}$ keV band, but little of the intensity seen in the higher energy bands, which must be produced by additional components.

Inferences that can be drawn from these maps about the spatial structure of the plasma responsible for the soft X-ray component strongly depend on the absorption of the X-rays by the interstellar medium (ISM). Since the photoelectric absorption cross section varies roughly as E^{-3}, our ability to detect X-rays from a significant distance away diminishes rapidly as the energy of the X-rays decreases (see, e.g., Morrison & McCammon 1983). One absorption optical depth corresponds to a column density of neutral hydrogen, $N_{\rm H} \sim 10^{20}$ cm^{-2} for X-rays in the $\frac{1}{4}$ keV band, to $N_{\rm H} \sim 5 \times 10^{19}$ cm^{-2} for B band X-rays, and to $N_{\rm H} \sim 10^{19}$ cm^{-2} for Be band X-rays.

Thus the ISM is opaque at low Galactic latitudes, $|b| \lesssim 30^\circ$, and the finite intensity of the X-ray background at low latitudes must be Galactic in origin and originate relatively near to the Sun, within the closest $\sim 10^{20}$ cm^{-2} $N_{\rm H}$. At high Galactic latitudes in the directions of lowest $N_{\rm H}$, the ISM transmission rises to $\sim$60% for $\frac{1}{4}$ keV X-rays and to $\sim$37% for B band X-rays, but is still less than 1% for Be band X-rays. The total $N_{\rm H}$ is $\lesssim 3 \times 10^{20}$ cm^{-2} over $\sim$ 25% of the sky, and significant contributions to the $\frac{1}{4}$ keV band from extragalactic or halo sources are possible in addition to the local emission. The detection by the *ROSAT* observatory of "shadows" in the X-ray background, localized negative correlations between the X-ray surface brightness and the ISM column density, indicates that in some high-latitude directions one-half to two-thirds of the observed $\frac{1}{4}$ keV diffuse background X-rays originate in the halo or beyond (Burrows & Mendenhall 1991; Snowden et al. 1991).

The location of the plasma responsible for the local component of the soft X-ray diffuse background is presumed to be a cavity in the local ISM that contains the Sun. Observations of Lyα and neutral sodium absorption lines towards

[1] Css: Harvard–Smithsonian Center for Astrophysics, 60 Garden Street, Cambridge, MA 02138.

stars within 300 pc reveal that the Sun is located inside a low-density interstellar cavity in the Galactic plane surrounded by a denser neutral gas boundary at a distance of roughly 120 pc, plus or minus a factor of 2 (Welsh, Crifo, & Lallement 1998; Sfeir et al. 1999). The plasma does not necessarily extend to the cavity walls in all directions in the plane, but it may extend into the halo at high Galactic latitudes (Snowden et al. 1998; Welsh et al. 1999).

1.2. *Spectral Characteristics*

Knowledge of the spectral characteristics of the low-energy X-ray background has been limited by the energy resolution ($E/\Delta E \sim 1$) of the proportional counters used in the all-sky surveys and in other attempts to measure the diffuse X-ray background spectrum. Additional spectral information comes from the ratios of the count rates in the energy bands defined by the K-edge filters of Be, B, and C referred to earlier. The observed proportional counter pulse-height distributions and the broadband count rate ratios of the Be, B, and C bands are consistent with those predicted from a plasma in ionization equilibrium at a temperature near one million degrees, independent of the particular model used. Since no viable nonthermal mechanisms are apparent (Williamson et al. 1974), and there are reasons to think that the $\frac{1}{4}$ keV diffuse background could have a thermal origin (e.g., fossil supernovae; Cox & Smith 1974), the usual interpretation of the $\frac{1}{4}$ keV diffuse background is that it originates from a million degree plasma, known as the "Local Hot Bubble" (Cox & Reynolds 1987; Snowden et al. 1990, 1998), located in the local cavity in the ISM.

Models of the X-ray emission of such a hot (10^5 K $< T < 10^7$ K) plasma typically find that almost all of the power is in emission lines. In the $\frac{1}{4}$ keV band, it is expected that most of the emitted power should appear in the lines of highly ionized Si, Mg, and Fe, if the elemental abundances are approximately solar. If refractory elements such as these are depleted in the hot gas (e.g., contained in dust grains), as they often are in cooler regions of the ISM, lines of Ne, S, and Ar should dominate instead. In any case, a spectrometer that is sensitive to diffuse X-ray emission is needed to study the wealth of detail that is accessible in these lines about the state and history of the plasma.

2. INSTRUMENT DESCRIPTION

The Diffuse X-ray Spectrometer (DXS) experiment consists of a pair of Bragg-crystal spectrometers designed to obtain spectra of the diffuse X-ray background in the 84–44 Å (148–284 eV) range, with spectral resolution $\lesssim$2.2 Å (4 eV at 148 eV to 14 eV at 284 eV), and angular resolution $\sim$15°. The primary objective of this experiment was to search for emission lines in the spectra of the diffuse background to verify its thermal origin, and to determine the physical condition of the hot material. Although the spectrum was expected to consist of line blends as well as lines, comparison with model predictions could provide information about the plasma temperature, elemental abundances, ionization states, and history. The isotropy of these spectral characteristics over a limited region of the sky could also be investigated.

2.1. *Physical Description*

The DXS detector conceptual design was described by Borken & Kraushaar (1976). Detailed descriptions of the flight instrument are given by Sanders et al. (1992, 1993), Morgenthaler (1998), and references therein. Figure 1 shows a cross-sectional view of a DXS detector assembly. Magnets were located at the entrance aperture of each spectrometer to reject low-energy ($E < 20$ keV) electrons, both because such electrons can generate extraneous X-rays from surfaces that they hit, and because low-energy electrons that enter the proportional counter can generate pulses that mimic low-energy X-ray events. The aperture seal/baffle keeps out light, particularly solar ultraviolet, while the instrument is stowed.

The detector has three major components: the 63.3 cm radius X-ray reflecting crystal panel, the collimator, and the one-dimensional position-sensing proportional counter. Each Bragg crystal panel consists of four thin rectangular plastic sheets (0.1 cm × 15 cm × 36 cm) mounted next to each other (out of the page in Fig. 1) whose surfaces are coated with 200 layers of lead stearate (PbSt), producing a one-dimensional pseudocrystal with a $2d$ spacing of 101.5 Å. The geometry of the crystal panel and collimator is such that photons Bragg-reflected from the curved crystal panel are directed toward the position-sensing proportional counter with the longer wavelength photons striking it on one side and the shorter wavelength photons on the other, thus providing spectral dispersion across the counter. The collimator limits the photons entering the proportional counter to those traveling within 15° (FWHM) of the line perpendicular to the entrance window of the proportional counter in both the dispersion and cross-dispersion directions, so that there is 15° × 15° angular resolution at each wavelength. While most of the crystal panel area is used at all wavelengths, Bragg reflection does not allow true multiplexing, and photons of different wavelengths enter the instrument from different directions on the sky, as pictured schematically in Figure 1. In order to collect photons of all energies of the instrument bandpass from the same sky direction, the detector assembly must be rotated through an angle of 65°.

The DXS experiment flew as an attached payload on the STS-54 mission of the space shuttle *Endeavour* in 1993 January. Figure 2 shows the port *DXS* instrument in its stowed position mounted on the side of the shuttle cargo bay. The starboard instrument was located on the other

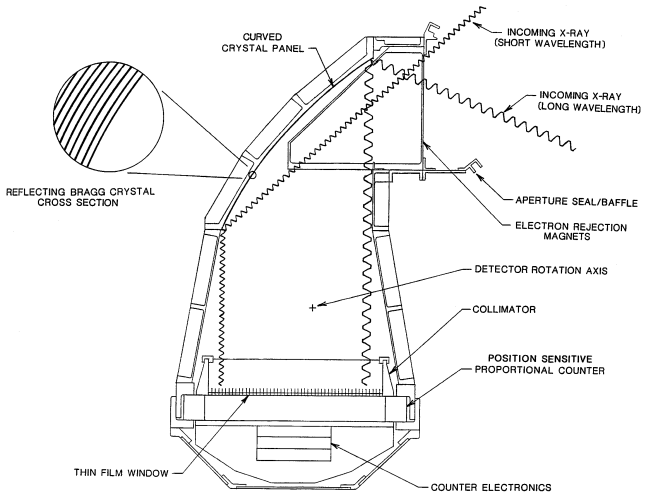

FIG. 1.—Cross-sectional view of a DXS detector showing photon paths and some of the detector's major parts. The X-ray reflecting crystal panel is made of 200 layers of lead stearate.

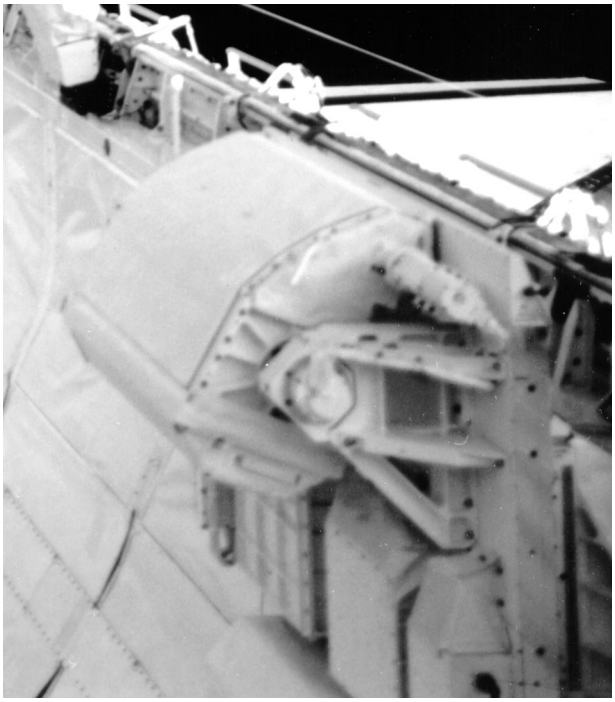

FIG. 2.—Port DXS instrument in its stowed position mounted to the side of the Orbiter cargo bay. The outside of the curved crystal panel is visible, with the proportional counter attached below it. The Orbiter port wing is visible in the background.

side of the Orbiter, directly across from the port instrument. When collecting sky data, the instruments rotated back and forth every two minutes, detecting X-ray photons from an arc on the sky 15° (FWHM) wide, defined by the collimator, and 167° long, limited by the sills of the Orbiter cargo bay. This arc was perpendicular to the roll (tail to nose) axis of the Orbiter and was centered near the Orbiter yaw axis (perpendicular to the plane of the Orbiter wings). For all DXS data collection intervals during the mission, the Orbiter maintained the same inertial attitude to within a few degrees, so that each DXS detector repeatedly scanned nearly the same arc on the sky. Because the PbSt may be destroyed by solar ultraviolet radiation and also by atmospheric oxygen atoms hitting it at the Shuttle orbital velocity, the DXS detectors scanned only during orbit night and then only when the Orbiter attitude was such that residual atmospheric oxygen was blocked by the Orbiter body from hitting the crystal panels directly.

The large area (30 cm × 60 cm) position-sensing proportional counters used in DXS are filled with P-10 gas, a mixture of 10% methane and 90% argon, regulated to a constant density corresponding to a pressure of 800 torr at 20 C. A thin (80–90 μg cm^{-2}) plastic window supported by a 100 lines-per-inch nickel mesh and the collimator structure retains the counter gas while allowing soft X-ray photons to enter the counter. The window is composed of Formvar ($C_5H_7O_2$, the registered trade name of the polyvinyl formal resin produced by Monsanto Chemical Company) with an additive, Cyasorb UV-24 ($C_{14}H_{12}O_4$, a trade name of American Cyanamide), to absorb stellar ultraviolet photons that could otherwise generate a large non–X-ray background. Once past the window, $\frac{1}{4}$ keV X-rays are absorbed photoelectrically in the first few mm of counter gas, producing a small cloud of electrons. The resulting charge cloud drifts toward the plane of 14 main anode wires, which are held at ~1700 V with respect to the counter body and run across the narrow dimension of the counter (along the spectrometer dispersion direction), 1.5 cm below the window. The initial charge is accelerated toward the main anodes and causes an electron avalanche when it is within a few microns of a main anode wire. The resulting charge pulse on the main anode is converted to a voltage pulse by a charge-sensitive amplifier. Below and perpendicular to the main anodes are 96 wires held at ground potential, attached to charge-sensitive amplifiers in groups of four. The induced charge distribution on the ground-plane wires is used to determine the position of the electron avalanche in the dispersion direction to $\leq$1 mm. Position determination is independent of main anode pulse height.

One anticoincidence anode is located at each end of the main anode plane, and a plane of anticoincidence anodes is located below the ground plane wires. In combination with position-sensing, this provides very efficient five-sided vetoing of penetrating charged-particle events. Laboratory and flight tests show that the residual non–X-ray background is consistent with cosmic rays converting to γ-rays in the materials surrounding the proportional counter, and these γ-rays Compton scattering in the counter gas where the scattered electron escapes through the window after depositing a small fraction of its energy in the gas. The resulting spectrum is flat across the proportional counter at an average level in the 0.1–0.45 keV interval of 1.6×10^{-4} s^{-1} cm^{-2} keV^{-1} (0.068 ± 0.0007 s^{-1} per detector), with variations in time of 0.5×10^{-4} s^{-1} cm^{-2} keV^{-1} (0.02 s^{-1} per detector) that depend on the Orbiter position relative to the Earth.

2.2. *Instrument Calibration*

In this section, we describe the DXS calibration measurements and estimate the accuracy of the instrument response functions that were created based on those measurements. Before the assembly of the DXS spectrometers, the properties of their components were measured, and a computer ray-tracing model was used to predict the spectrometer output as a function of incident photon energy. Measurements of the instrument response to a diffuse source were made at two wavelengths before the DXS flight, and at three wavelengths afterwards. Table 1 gives the particular lines and their nominal energies. These measurements were compared with the predictions of the preassembly model. Response matrices were then constructed to enable the prediction of both the measured spectrum and the measured pulse-height distribution for a specified spectrum of incident X-rays. These response functions are logically divided into two separate functions. The photon detection efficiency function predicts how many counts are detected per incident photon cm^{-2} sr^{-1}, and the count redistribution matrix predicts how those counts are distributed in pulse height and, for a spectrometer, in position. In the nomenclature of the widely used X-ray spectral fitting program, "xspec" (Arnaud 1996), the photon detection efficiency function is the auxiliary response file (arf) and the count redistribution matrix is the response matrix file (rmf).

2.2.1. *Area–Solid Angle Product ($A\Omega$) Calibration*

Because the amount of emission from a diffuse source is characterized by its surface brightness (e.g., units of photons

TABLE 1

α-PARTICLE–EXCITED X-RAY CALIBRATION SOURCES

Target	Line	E (eV)	λ (Å)	Preassembly	Preflight	Postflight
Zirconium	M-ζ	151	82.1	No	No	Yes
Boron	K-α	183	67.6	Yes	Yes	Yes
Carbon	K-α	277	44.8	No	Yes	Yes

s^{-1} cm^{-2} sr^{-1}) in a wavelength interval, the appropriate measure of an instrument's response to a diffuse source is its effective area–solid angle product ($A\Omega$, in units of cm^2 sr counts photon^{-1}, or simply cm^2 sr). When expressed as a function of incident photon energy, $A\Omega$ is the photon detection efficiency function described above. The calculation of the DXS $A\Omega$ function is described in detail by Morgenthaler (1998).

The X-ray reflection properties of lead-stearate crystals similar to those used in DXS were studied using a grating monochromator attached to the Tantalus II synchrotron light source at the University of Wisconsin's Physical Sciences Laboratory (PSL). At three energies across the DXS bandpass (151, 183, and 277 eV), the X-ray reflectivity of lead stearate was measured as a function of angle and polarization. Reflectivity at 277 eV was also measured in second order, and higher order Bragg reflection from Al K-α and O K-α was studied in our laboratory. The reflectivity of the crystal as function of angle at a particular energy was characterized as the sum of a narrow Gaussian, a wide Gaussian, and a one-sided Lorentzian, plus a specular reflection component. Parameters describing these components were determined as a function of energy and were incorporated into a ray-tracing program that calculated the instrument response up to the proportional counter window.

The proportional counter window transmissions were measured as a function of energy both preflight and postflight. The postflight window transmission was measured at 21 (port) or 32 (starboard) separate positions on the window to quantify thickness nonuniformities, but the window transmissions were found to be uniform to $\lesssim 4\%$ with no apparent large-scale structure. Window transmission was modeled as a function of energy using X-ray absorption coefficients of Henke et al. (1982) and the atomic composition of the constituent window materials, 66 μg cm^{-2} Formvar and 20 μg cm^{-2} UV-24. The measured and modeled transmissions of the port instrument flight window are shown in Figure 3. The UV-24 thickness was determined independently by weighing and from the X-ray transmission of typical UV-24 layers, and the Formvar thickness was adjusted to fit the measured transmission data. The modeled transmission as a function of energy is not at all sensitive to the relative thicknesses of Formvar and UV-24, since their atomic compositions are so similar.

Using the proportional counter pulse-height model of Jahoda & McCammon (1988), the efficiency of the DXS proportional counters in detecting pulses corresponding to photons of a particular energy was calculated. For the analysis of the DXS port flight data, the lower level discriminator setting was 104 eV and the upper level discriminator was 405 eV. Figure 4 shows the pulse-height detection efficiency function for the port instrument determined with these discriminator settings. The low efficiency at low energies is due to the broad proportional counter pulse-height response distributing counts below the lower level discriminator, while the falloff at high energies is due to counts being similarly distributed above the upper level discriminator. The efficiency decreases at 50.6 Å and at 43.7 Å are caused by discontinuous changes in the shape and mean energy of the pulse-height distributions at the argon-L edge

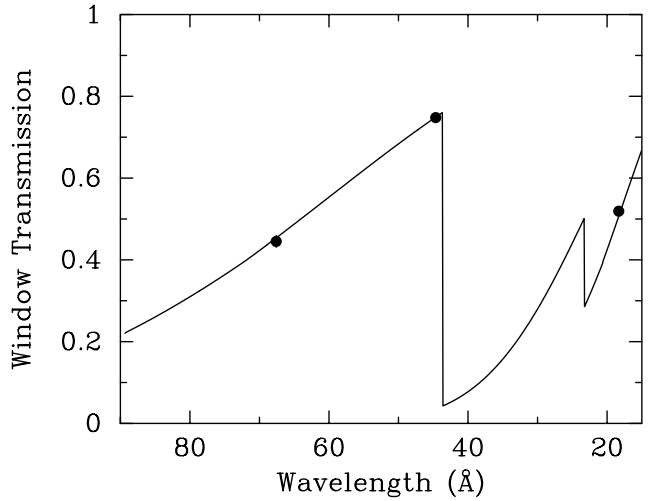

FIG. 3.—Measured (*data points*) and modeled (*solid line*) port flight window transmission as a function of wavelength. The Formvar thickness of the model was adjusted to fit the measured data. The transmission decreases at 44 and 23 Å are caused by increased absorption of the plastic window at the carbon-K edge and the oxygen-K edge, respectively.

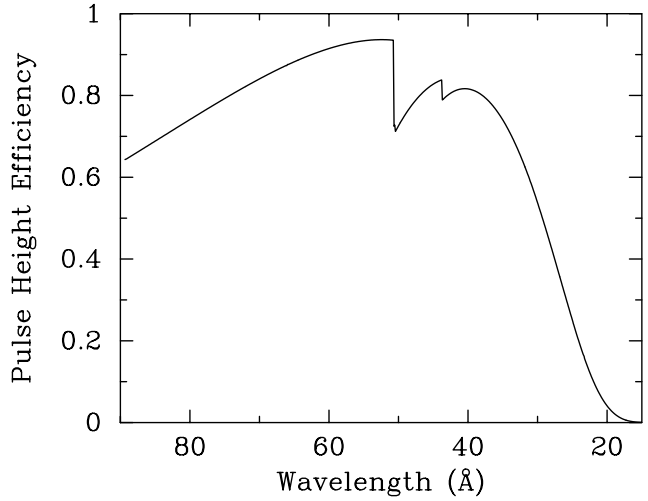

FIG. 4.—Port proportional counter pulse-height detection efficiency resulting from the pulse-height limits used for the analysis of the flight data. The efficiency decreases at 51 and 44 Å are caused by changes in the pulse height distributions at the argon-L edge and the carbon-K edge, respectively, of the absorbing P-10 gas.

and the carbon-K edge, respectively, of the absorbing P-10 gas (Jahoda & McCammon 1988).

End-to-end measurements of the effective $A\Omega$ of DXS were made in the laboratory preflight at two energies and postflight at three energies using diffuse X-ray sources produced by α-particle fluorescence from carbon, boron, and zirconium targets. Table 1 gives the particular lines and their nominal energies. As discussed in § 2.2.2, the chemical environment of the target atom can broaden and shift the actual spectrum from the fluorescent target. A sheet of each target material large enough (35 cm × 50 cm) to intercept all lines of sight to the detector in the dispersion plane over a limited range of cross-dispersion positions was used. It was exposed to an array of ^{210}Po α-particle sources positioned so as to produce a fairly uniform surface brightness of fluorescent X-rays from the target. To simulate illumination of the full DXS aperture with this diffuse X-ray source, exposures of it were taken at sixteen positions spanning the DXS detector aperture. From these exposures, the total DXS count rate that would be measured by the entire counter from a diffuse source filling the DXS aperture was determined.

The absolute calibration of the diffuse sources was performed using a small proportional counter with a well-defined area and a well-measured window. This counter was used to measure the surface brightness of the targets from 4 or 5 different strips across the target at typically 5 angles in either of two orthogonal directions from the normal. Corrections were made for the decrease of the ^{210}Po source strength over the course of these measurements due to its 138 day radioactive half life. The ratio of the DXS count rate over the full wavelength range of the instrument to the target surface brightness is the DXS $A\Omega$ measurement for a given energy of fluorescent line.

Figure 5 shows the DXS port instrument $A\Omega$ measurements, preflight at two energies (*open circles*) and postflight at three energies (*filled circles*). The postflight values are 5%–6% lower than the preflight values, differences that are within the 1 σ uncertainties of the measurements. Where more than one value is displayed at the same energy, the most recent value is plotted at the nominal energy and the earlier values are offset to the left for clarity.

The dashed line in Figure 5 shows the model $A\Omega$ function calculated using the preassembly measurements of the

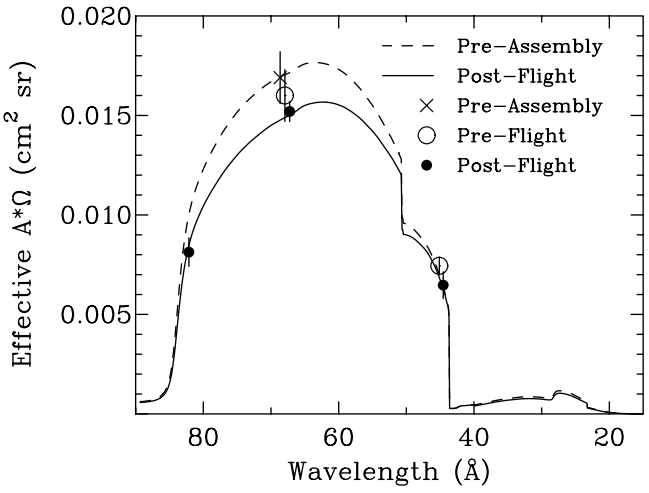

FIG. 5.—DXS port instrument $A\Omega$ measurements (data points) and model $A\Omega$ functions (*lines*).

window thickness and of the reflectivity of the individual port instrument Bragg-crystal sheets (measured at one place on each sheet), the ray-tracing model of the instrument geometry, and the proportional counter pulse-height model (Jahoda & McCammon 1988). There are no free parameters in this model. The error bar at 68 Å attached to the "x" data point indicates the 10% uncertainty estimated for the integrated reflectivity measurements of the sheets. The solid line shows the postflight port model $A\Omega$ function, where the crystal integrated reflectivity has been reduced by ~12% to better fit the measured data. The energy dependence of the crystal reflectivity was also adjusted slightly so that the net effect of both adjustments was to decrease the integrated reflectivity by a factor that varied from 10% at 42 Å to 14% at 85 Å. For the postflight model then, two adjustable parameters were varied to fit three data points, resulting in a fit with 1 degree of freedom (dof). The crystal second-and third-order reflectivities are incorporated in the model $A\Omega$ functions, although the data upon which they are based are not very extensive (see § 2.2.4). The postflight $A\Omega$ model is used for the scientific analysis presented here.

2.2.2. *Wavelength Calibration*

The $A\Omega$ measurements yielded not only a determination of the efficiency of the instrument, the number of counts per photon cm^{-2} sr^{-1}, but also a high statistical precision record of the distribution of those counts in position. In combination with the ray-tracing program and the lead-stearate rocking curves measured at PSL, these data were used to create the response matrix that describes the count distribution in position. The count distribution has two main characteristics: the shape of the distribution and the location of the centroid of the counts for a given photon energy. The wavelength calibration is concerned with the latter.

The ray-tracing program in conjunction with the PSL rocking curve data was used to calculate the expected position profile on the detector for each wavelength. The position of the peak for a given wavelength is determined by the $2d$ spacing of the lead stearate and the geometry of the DXS instrument, which is known to within the mechanical tolerances of a few tenths of a mm. Henke et al. (1982) give the $2d$ spacing of lead stearate as 100 Å, but our PSL rocking curve measurements are better fitted by 101 Å, and measurements of the spectrum of higher order Bragg reflection peaks of Al K-α give a $2d$ value of 101.5 Å. Comparison of the spectra measured in the $A\Omega$ determinations to the predictions of the calculated response matrix with different assumed values of $2d$ showed that $2d = 101.5$ Å gave the best agreement.

Comparison of the measured spectrum to that predicted by the detector model is complicated because the photon spectra arising from the α-particle–excited sources of Table 1 depend on the chemical environments of the excited atoms and are not precisely known. Several examples of such spectra measured at high resolution are found in the literature (e.g., Bastin & Heijligers 1992; Holliday 1967; Skinner 1940) and were used as trial input photon model spectra for comparison to the measured data. Using a response matrix based on a value of $2d = 101.5$ Å, we find that the central peak of our measured carbon K-α line is well fit by the TiC spectrum from Holliday (1967) if the latter is shifted 0.4% to shorter wavelengths. It is also well fitted by a Gaussian line with a mean of 44.6 Å (278 eV) and

$\sigma = 0.5$ Å (3 eV), which is 0.16 Å shorter wavelength (1 eV higher energy) than the nominal value (44.76 Å, 277 eV) for the carbon K-α line (Henke et al. 1982). Our data show a long wavelength tail, extending to ~ 60 Å, that is not seen in the Holliday (1967) TiC spectrum, and is not present in our monochromator measurements at PSL.

Our measured boron K-α line also has a long wavelength tail extending to ~ 75 Å, similar to those seen in other boron K-α spectra (e.g., Bastin & Heijligers 1992; Holliday 1967; Skinner 1940), but the central peak appears to be intrinsically narrower than that of Holliday (1967), which is the narrowest elemental boron K-α line profile of those found in the literature. Using the same $2d = 101.5$ Å response matrix and allowing for the shape differences, we find that the centroid of our measured boron profile is shifted 0.4% toward shorter wavelengths compared to that of Holliday (1967). In addition, the central core and short wavelength side of our boron profile can be reasonably fit by a Gaussian line with a mean of 67.84 Å (182.8 eV) and $\sigma = 0.6$ Å (1.5 eV), which is 0.2 Å longer wavelength (0.5 eV lower energy) than the nominal value (67.64 Å, 183.3 eV) for the B K-α line (Henke et al. 1982).

The zirconium M-ζ line profile was not found in the literature, but the main peak of our measured spectrum is quite narrow and is consistent with a Gaussian line shape with a mean of 82.1 Å (151 eV) and $\sigma \leq 0.3$ Å (0.6 eV). Our zirconium M-ζ spectrum also shows a short wavelength tail extending to less than 70 Å, with some structure possibly due to weaker zirconium M lines. The value of $2d = 101.5$ Å was adopted for the DXS response matrix because it fitted the higher order Bragg reflection peaks of the Al K-α line and it gave the correct position for the Zr-M line, which was intrinsically narrow enough that uncertainty in the line profile as excited from a solid could not affect the peak position.

The solid line of Figure 6 is the product of the DXS response matrix and the sum of the three input functions, TiC (Holliday 1967), B (Holliday 1967), and an 82.1 Å (151 eV) zero-width Gaussian. The data points are the three DXS postflight calibration spectra from the carbon, boron, and zirconium targets, and illustrate well the tails discussed above that are associated with the lines. For this figure, the normalizations of the three input model functions were independently varied to obtain the fits to the data, but the wavelengths were not shifted. If these input functions are fit to the measured data with the normalization factors *and* wavelengths as variable parameters, the maximum wavelength adjustment required for the best fit for any of the three input models is 0.2 Å. We therefore adopt 0.2 Å as the accuracy of our wavelength scale.

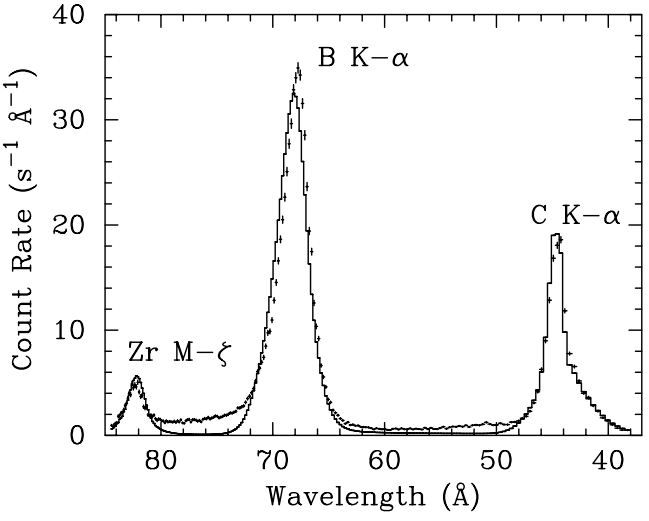

FIG. 6.—Spectral model comparisons (*solid line*) with three DXS postflight calibration spectra (data points with error bars). The zirconium M-ζ input model function is a 151 eV delta function. The carbon K-α and boron K-α input functions are the unshifted spectra from Holliday (1967). The Holliday boron line profile appears to be broader than the boron source used in the DXS calibration.

2.2.3. *Resolving Power*

Using the DXS spectral response function, we can calculate the resolving power, $\lambda/\Delta\lambda$ (FWHM), as a function of wavelength. The results of this calculation are shown in Figure 7. The measured resolving powers of the instrument from the laboratory calibration sources are also plotted on this figure. The boron and carbon points are shown as lower limits because these lines are resolved by DXS. The DXS resolving power of 25–40 is a factor of 10–20 better than the resolving power of the proportional counters used in the *ROSAT* and Wisconsin all-sky surveys at these energies.

2.2.4. *Higher Order Reflections*

A dispersive spectrometer has the feature that high-order spectra fall on the same places on the detector as the first-order spectrum, and may confuse the interpretation. Although the higher order calibration is less certain, the DXS $A\Omega$ function includes sensitivity for second and third order reflections, based on the PSL measurement of the 44.8 Å (277 eV) line in second order, and on our measurements of second and third order reflectivity for the O K-α and Al K-α lines. The contribution from higher orders is reduced both by the rejection of counts with pulse heights outside the 104–405 eV interval defined by level discriminators (see Fig. 4), and by the increased photoelectric absorption in the proportional counter window of photons in the 43.7–20 Å (284–600 eV) range. These effects are accounted for in the $A\Omega$ function. Models of the diffuse X-ray background combined with the DXS response predict that the higher orders produce less than 2% of the total counts observed in the

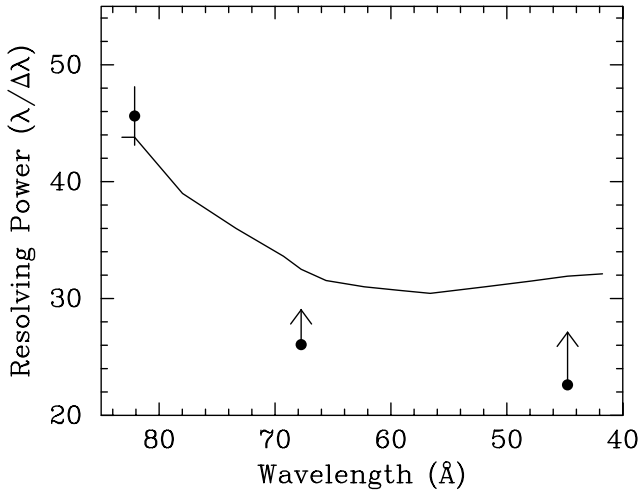

FIG. 7.—Calculated resolving power $\lambda/\Delta\lambda$ (FWHM) with measured points. The boron (67.6 Å) and carbon (44.8 Å) points are shown as lower limits, because the lines are clearly resolved by the instrument.

spectrum, and less than 7% of the counts in any position bin (see § 4.6).

3. DATA COLLECTION AND REDUCTION

3.1. *Flight Operations*

DXS observed a swath of the sky ~15° (FWHM) wide and ~167° long roughly aligned with the Galactic plane and centered at a Galactic longitude of ~ 225°. This scan path covers regions of the sky typical of the diffuse X-ray background as well as the Vela and Monogem supernova remnants. Figure 8 shows the DXS port instrument exposure pattern superimposed on the $\frac{1}{4}$ keV map of the *ROSAT* all-sky survey (Snowden et al. 1997).

During each shuttle nighttime pass, the DXS detectors were rotated from their stowed positions and scanned 8–10 times across the region of the sky shown in Figure 8. The proportional counter high voltage was turned on a few minutes before each scan period and left on for a few minutes afterwards for instrument background measurement. Before and after each scan, the proportional counter gas gains were measured using an on-board aluminum-anode X-ray tube. A charge pulser was used to measure the amplifier electronic gains and offsets several times during the mission.

The amplifier gains and offsets remained steady to within 0.5% throughout the flight, but the proportional counter gas gain decreased by about 20% over the course of the mission. The pulse heights were gain-corrected by multiplying the measured pulse height by the ratio of the nominal aluminum K-α pulse height to the average aluminum K-α calibration pulse height for that orbit. The pulse heights were also corrected for position-dependent gain variations across the counter. Software upper and lower discriminator levels were applied to select a fixed range of corrected pulse heights, so that the detection efficiency was independent of gain. This required choosing a software lower discriminator level high enough in corrected pulse height, 104 eV, that it never was less than the value of the corrected hardware lower discriminator, which was 70 eV at the nominal gain.

Breakdown in the starboard proportional counter has made extraction and interpretation of usable data from the starboard instrument difficult (Morgenthaler 1998). The amount of usable data from the starboard counter is less than half that from the port counter, and although the starboard data are consistent with the port data, their inclusion in these analyses would introduce systematic uncertainties greater than the decrease in statistical uncertainties. For these analyses we consider only data from the port instrument. Figure 9 shows a plot of the total count rate as a function of time in the port instrument. The count rate of orbits 51–90 is 17% less than the count rate of orbits 7–50, an effect that is not understood. After eliminating other possible causes (cosmic rays, soft electrons, gas amplification gain, pulse-height distribution shape, electronics deadtime correction, occultation of the instrument aperture, atmospheric absorption, or change in instrument sensitivity), Morgenthaler (1998) suggests that a long term enhancement (LTE; see Snowden et al. 1995), similar to those observed during the *ROSAT* All-Sky Survey may be responsible. LTEs appear to be due to X-rays that originate between the Earth and the Moon, that can occasionally be

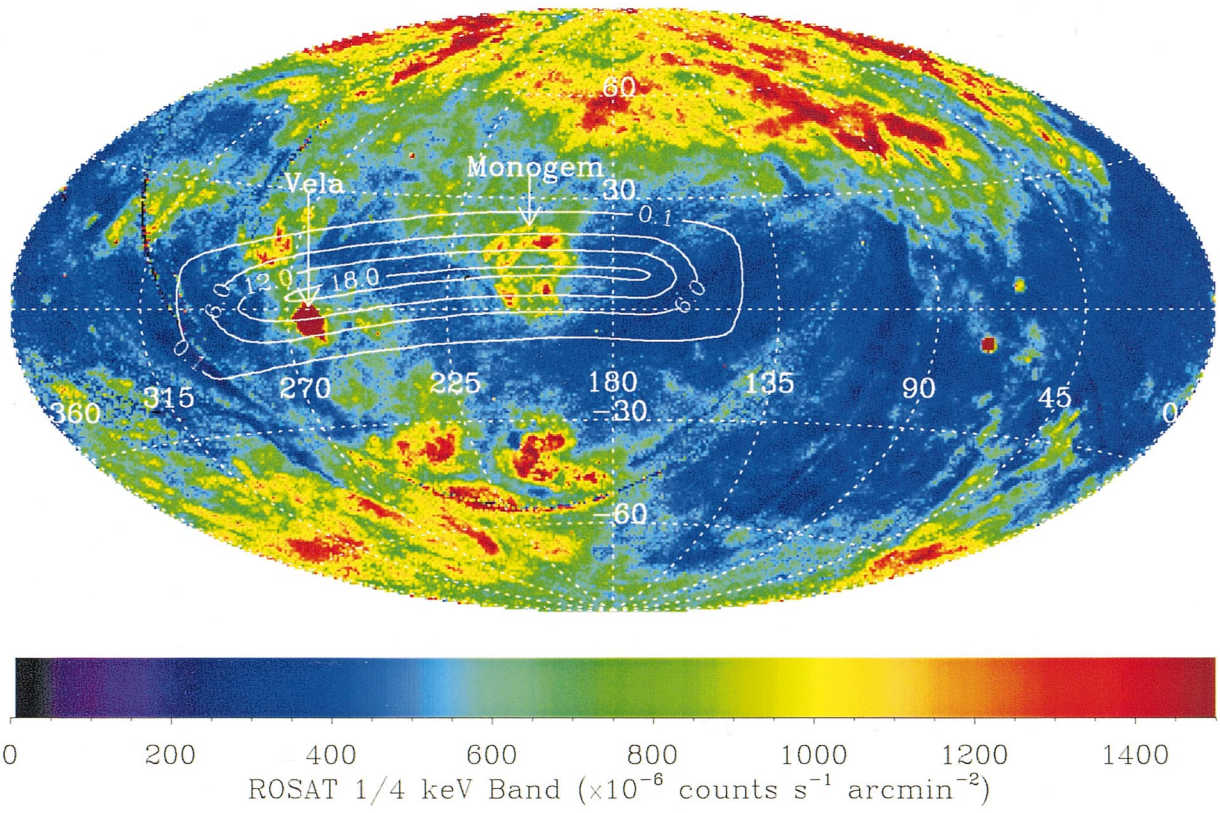

FIG. 8.—*ROSAT* all-sky survey (Snowden et al. 1997) $\frac{1}{4}$ keV band map with contours of the exposure pattern of the port DXS instrument. The map is an Aitoff projection, centered at 180° Galactic longitude. The units of the DXS exposure are seconds per 1° × 1° pixel, and contours are shown at 0.1, 6.0, 12.0, and 18.0 s.

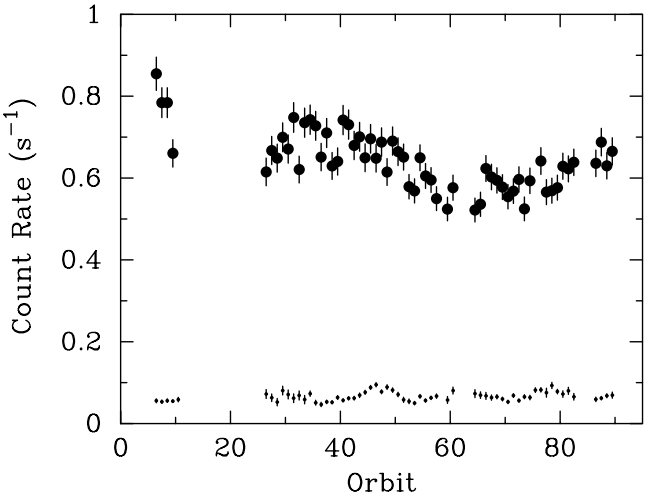

FIG. 9.—Time history of the total count rate, including background, in the port instrument (upper set of points). The instrument background rate, which was measured when the instrument was stowed, is shown separately by the lower set of points, and averages 0.068 s^{-1} (1.6×10^{-4} s^{-1} cm^{-2} keV^{-1}). Each orbit is approximately 91 minutes.

as strong as the cosmic background in the $\frac{1}{4}$ keV band, that may last for days, that are uncorrelated with orbital or geographic parameters, and for which no physical mechanism has been determined. The only DXS parameter that shows a behavior similar to the count rate decrease is the port detector gas gain, which shows a 13% drop after orbit 41 compared to prior orbits, but this gas gain is only slightly correlated with the count rate. Regardless of the cause of the changing count rate, the average count rate was used for the analysis presented here.

3.2. *Data Reduction*

Although an arc of the sky 167° long was visible from the locations of the DXS detectors, the 15° (FWHM) field of view was partially occulted by the upper part of the Orbiter cargo bay wall at either end of that arc, so that only 137° of the DXS scan, $297° > l > 160°$, was fully exposed. The 30° arcs at either end of the scan path, $327° > l > 297°$ and $160° > l > 130°$ are partially occulted, and the data from these directions are not used in the spectral analysis here. Since a DXS detector must execute a complete 65° scan across a sky direction to obtain full wavelength coverage from that direction, the ends of the scan path have only partial wavelength coverage. Thus, the wavelength coverage increases from no coverage at $l \approx 336°$ to full coverage at $l \approx 271°$, and decreases from full coverage at $l \approx 175°$ to no coverage at $l \approx 110°$. Since the detector is already fully occulted for $l < 130°$ and $l > 327°$, the scanning data in these ranges provide an independent measurement of the detector background.

For the DXS data analysis, counts were selected whose corrected pulse heights were in the range 104–405 eV with spectral positions in the 84–42 Å (148–295 eV) range, and whose charge distributions across the position-sensing ground plane wires were consistent with the expected shape. To create a one-dimensional map of the sky brightness measured by DXS, the data satisfying these criteria were projected onto the sky. For each of 200 spectral positions across the position-sensitive proportional counter, detected counts and exposure times were accumulated into one-dimensional arrays of bins along the DXS scan path. For each 1 s time interval, for each position along the counter, the appropriate direction on the sky was determined, and the detected counts and the live time were added to the 1° wide bin containing the center of the field of view at the middle of the time interval. For this display, spectral information was not retained. The count array was divided by the exposure array to give counts s^{-1} position^{-1}, and this was multiplied by the 200 positions per detector to yield a one-dimensional map of count rate, including background. This count rate is really an "equivalent" count rate, since ignoring spectral information results in nonuniform spectral weighting where the wavelength coverage is not complete at Galactic longitudes greater than 271° and at Galactic longitudes less than 175°. The data points on the lower plot in Figure 10 show the equivalent count rate as a function of Galactic longitude, and the solid line of the upper plot gives the Galactic latitude of the center of the field of view as a function of Galactic longitude.

The DXS data were divided into sets defined by intervals along the scan path that correspond to five different regions on the sky. Figure 10 indicates the boundaries of those regions. The residual instrument background rate of 0.068 s^{-1} (1.6×10^{-4} s^{-1} cm^{-2} keV^{-1}), caused mainly by cosmic rays, is indicated as the dotted line in Figure 10. This background level was measured when the instrument was in its stowed position with the aperture completely covered. When the instrument scanned beyond the Crux or Auriga regions, where the shuttle cargo bay occulted the instrument field of view but the aperture was still open, the count rate fell to the same background level. This indicates that additional sources of background, such as low-energy electrons, are not present in the scanning data. The arrows in Figure 10 indicate the Galactic longitudes where the field of view was fully occulted by the Orbiter.

A model of the DXS angular sensitivity was approximated by propagating the 15° × 15° collimated field of view of each position on the counter through the same 38° Bragg reflection off the curved crystal panel onto the sky.

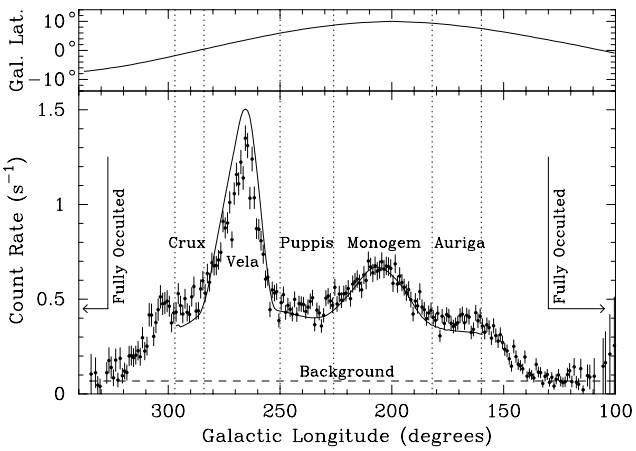

FIG. 10.—Effective count rate measured in the port DXS instrument as a function of Galactic longitude in 1° bins. Instrument background is included, and the background rate inferred from instrument-closed measurements is indicated by the dashed line. The solid line is a prediction of the DXS count rate based on the *ROSAT* $\frac{1}{4}$ keV band map (Snowden et al. 1995). The vertical dotted lines indicate the boundaries of the five regions selected for spectral extraction. Spectral coverage is incomplete for $l > 271°$ and $l < 175°$. The upper plot gives the Galactic latitude of the center of the field of view.

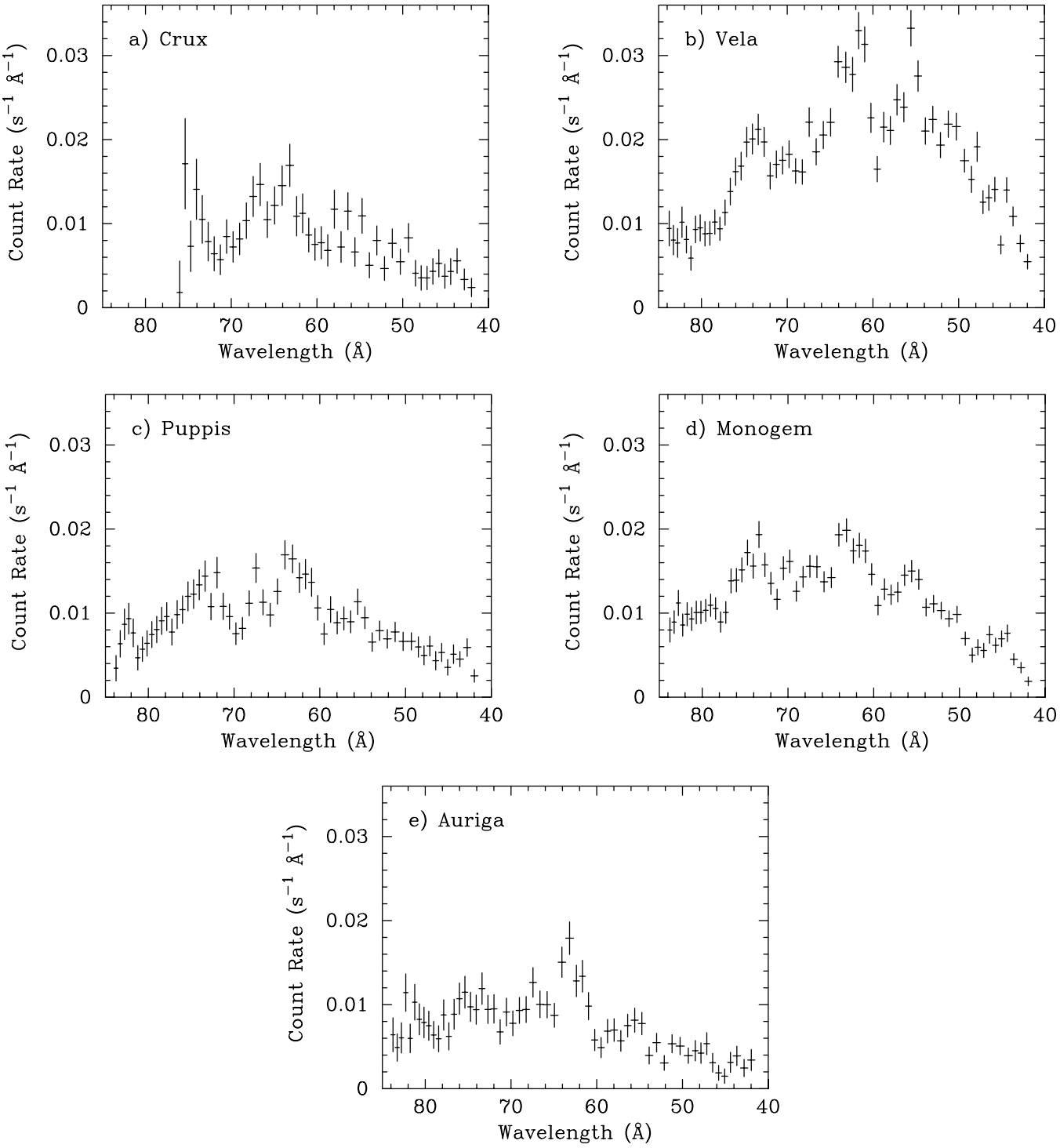

FIG. 11.—(*a*)–(*e*) DXS spectra from the five regions of the sky defined in Fig. 10. The Crux region was not observed by the port instrument at long wavelengths because the instrument was not rotated far enough to obtain that spectral coverage. The Vela and Auriga spectra have slightly reduced exposure at the longest and shortest wavelengths, respectively, for the same reason.

This sensitivity function was scanned across the *ROSAT* $\frac{1}{4}$ keV band map (Snowden et al. 1995) according to the DXS flight aspect data. The Snowden et al. (1995) map was used for this scan instead of the Snowden et al. (1997) map because point sources were removed from the latter map but not from the former. The resulting *ROSAT* count rates were scaled to produce a predicted DXS count rate using the ratio of the calculated count rate in the *ROSAT* $\frac{1}{4}$ keV band to that in the DXS 84–42 Å (148–295 eV) spectral range. This ratio, 1318, was determined using the model spectra of equilibrium plasma emission described in § 4.2, and varies only a few percent depending on the thermal spectral model type or its assumed elemental abundances. The solid curve on the lower plot in Figure 10 shows the sum of the *ROSAT*-predicted DXS count rate and the measured DXS non–X-ray background rate. Excluding the Crux and Vela regions, the *ROSAT*-predicted DXS count rate averages 10% lower than the measured DXS count

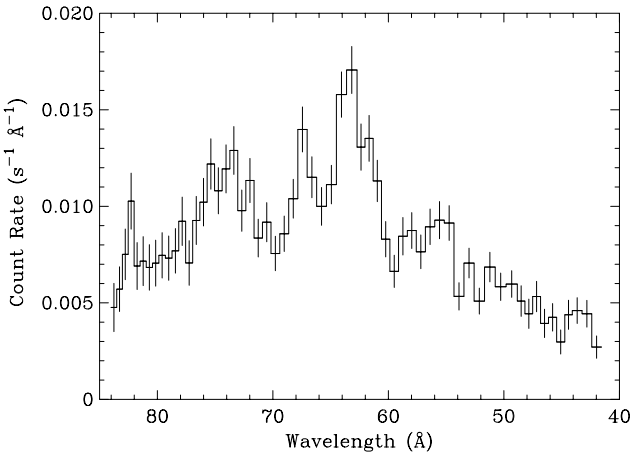

FIG. 12.—Spectrum of the hot interstellar medium (HISM) at low Galactic latitudes. This spectrum is the sum of the Crux, Puppis, and Auriga spectra shown in Fig. 11.

rate, consistent with the suggestion of Snowden et al. (1995) that the published effective area of the *ROSAT* $\frac{1}{4}$ keV band response function is about 10% high, although LTEs may contribute some excess DXS counts. The difference between the two rates in Vela appears to be due to the rather different X-ray spectrum of the Vela region, while in the Crux region it appears to be due to the incomplete spectral coverage and nonuniform spectral weighting at the ends of the DXS scans.

3.3. *Region-by-Region Spectra*

Spectra were extracted from each of the five regions indicated in Figure 10. These are shown in Figure 11 after non–X-ray background has been subtracted and flat-field corrections have been made. The partial wavelength coverage at the ends of the scans has negligible impact on the Auriga and Vela spectra, but results in the Crux spectrum having no spectral coverage longward of 76 Å. The Vela spectrum is clearly quite different from the others, and will be discussed in a subsequent paper (Morgenthaler et al. 2001, in preparation), along with the Monogem spectrum. Of the other spectra, Crux and Auriga are statistically indistinguishable, as indicated by a χ^2 test with no free parameters. When the Puppis spectrum is scaled to the same total count rate, no statistically significant difference in shape is found between it and the Crux and Auriga spectra. In order to simplify subsequent analysis and increase our statistical precision, we have combined the data from the Crux, Puppis, and Auriga regions to form a Hot Interstellar Medium (HISM) spectrum, shown in Figure 12.

4. DATA ANALYSIS

We have attempted to fit a range of simple and moderately sophisticated standard models to the DXS port instrument HISM spectrum and find no model that satisfactorily fits the data. Since this spectrum is a combination of the Crux, Puppis, and Auriga regions, and excludes the Puppis and Vela supernova remnants and the Monogem Ring (also a supernova remnant), the spectrum obtained is presumed to be typical of the low Galactic latitude diffuse background, dominated by X-ray emission from the Local Hot Bubble. We consider several classes of models. First we look at continuum spectra, then collisional equilibrium thermal spectra, and then we consider a class of nonequilibrium thermal models. We explore the reasons why such efforts fail, examining differences between X-ray emission codes.

4.1. *Maximum Flux Fraction due to a Smooth Continuum*

Although X-rays from the Local Hot Bubble are thought to arise from a million degree plasma whose emission consists almost totally of a large number of lines, this may not be true. As the DXS resolution is not sufficient to resolve all the lines that standard models suggest are present in its bandpass, it is possible that the spectrum consists of a smooth continuum underlying a few isolated lines. In order to assess the fraction of the observed flux that must come from spectral emission lines or other sharp spectral features, we have fit a power law to the DXS HISM spectrum. We then decreased the normalization of this power law until the modeled spectrum no longer exceeded the data at any point, giving 0.75 $E^{-3.2}$ photons s^{-1} cm^{-2} sr^{-1} keV^{-1}, where E is the energy in keV. The modeled flux equals that of the measured spectrum at several widely separated wavelengths, and is a good approximation to the greatest smooth continuum that may underlie the line spectrum. We find that this greatest smooth continuum can account for about 68% of the flux observed by DXS. Although there is no reason to think that it is not all thermal, as a very conservative lower limit, at least 32% of the 84–44 Å flux comes from sharp spectral features such as lines.

Another possible variety of continuum, from recombination processes, may contain step discontinuities at the ionization energies of the ions in the gas. Breitschwerdt & Schmutzler (1994) suggest that much of the diffuse X-ray background flux may come from recombination radiation. We therefore constructed a model consisting of recombination edges from ions present in plasmas at temperatures $\lesssim 10^7$ K. No combination of electron temperatures and recombination time scales produced a fit as good as the equilibrium thermal model fits discussed in the next section.

4.2. *Collisional Equilibrium Plasma Models*

Because X-rays from the Local Hot Bubble are thought to arise from a million degree plasma, collisional equilibrium thermal plasma models appear to be the natural models to fit to the DXS data. The appropriate elemental abundances for those plasma models are not obvious, however. Smith et al. (1996) show that dust-bearing gas heated to temperatures $\lesssim 10^6$ K will cool before most of the dust is sputtered. It is therefore possible that some dust survives in the hot gas responsible for the X-ray emission, which would result in depletion of refractory elements. This is in accord with the observations of Bloch (1988), Bloch, Priedhorsky, & Smith (1990), and Jelinsky, Vallerga, & Edelstein (1995), which suggest depletions of refractory elements within the X-ray–emitting gas, and with the fact that many supernova remnants, which emit strongly in X-rays, also emit strongly in the infrared owing to hot electrons interacting with dust grains (Dwek 1987). For the fits presented in this section, we consider three different sets of elemental abundances.

The intent of this section is to present fits of single temperature collisional-equilibrium ionization (CEI) plasma models to the DXS data. We found, however, that if we fit single temperature CEI models to the DXS spectral data alone, we can obtain good fits with models that violate

observational constraints at energies outside the DXS band. Typically, they make too many X-rays in the 0.5–1 keV band. To address this difficulty, we instead fit a more complete model of the diffuse X-ray background to the DXS data and simultaneously to the Wisconsin sky survey data (seven broad bands covering 0.13–6 keV; McCammon et al. 1983) to constrain the X-ray fluxes at higher energies. A three-component model has been used previously to fit the diffuse background at X-ray energies up to several keV: an unabsorbed thermal equilibrium model where $T \approx 1 \times 10^6$ K; an absorbed thermal equilibrium model with a temperature higher by a factor of 2–3; and an absorbed power law of the form 11 $E^{-1.4}$ photons s^{-1} cm^{-2} sr^{-1} keV^{-1}, where E is in keV (Burstein et al. 1977; Burrows 1982; Garmire et al. 1992; Kuntz & Snowden 2000). Accordingly, we simultaneously fit the DXS HISM spectrum, the DXS pulse-height distribution, and the Wisconsin sky-survey band count rates (McCammon et al. 1983) with a model of the form

$$M = E_{m,1}\,\Lambda(T_1) + e^{-\sigma N_{\rm H}}(E_{m,2}\,\Lambda(T_2) + 11E^{-1.4})\,, \quad (1)$$

where $\Lambda(T_i)$ is a thermal plasma emission model in coronal equilibrium at temperature T_i, $E_{m,i} \equiv \int n_e^2\, dl$ is the emission measure for gas with temperature T_i, $N_{\rm H}$ is the column density of neutral hydrogen (here assumed to be 1×10^{21} cm^{-2}), and σ is the energy-dependent interstellar medium cross section (Morrison & McCammon 1983). The fitting was done with the "xspec" program (Arnaud 1996) using two different thermal plasma emission model codes, that of Raymond & Smith (1977), as updated in 1993, hereafter RS and that of Mewe, Kaastra, & Liedahl (1995), with $\frac{3}{4}$ keV band iron emission computed by Liedahl, hereafter MEKAL. The energy resolution of the RS model was increased by recomputing it on 0.5 eV energy bins across the DXS bandpass (including high orders). These models are discussed further in § 4.4.

In our fits, we studied three cases of elemental depletions for the unabsorbed (local) component: (1) solar abundances of Anders & Grevesse (1989) with no depletions; (2) solar except for Mg, Si, and Fe, whose relative depletion was kept the same but allowed to float freely (labeled MgSiFe in Table 2); and (3) solar except for Mg, Si, and Fe, whose relative depletions were allowed to independently float freely (labeled "variable" in Table 2). These three elements were selected because they are refractory, abundant, and have many lines in the 84–44 Å band. We summarize the results of our fits of the model described by equation (1) to the DXS and Wisconsin sky survey data in Table 2 and Figures 13 and 14. In no case is the reduced χ^2 statistic less than 2.7, so none of the fits is formally acceptable, but visual inspection of Figure 14 indicates that the variable abundance MEKAL model is a good approximation. For any of the fits, the unabsorbed lower temperature model component provides more than 95% of the observed counts in the DXS band, and is effectively the best fit of a single-temperature collisional-equilibrium model to the DXS data.

TABLE 2

EQUILIBRIUM PLASMA EMISSION MODEL FIT PARAMETERS

Model[a]	kT_1 (keV)	$E_{m,1}$ (10^{-3} cm^{-6} pc)	kT_2 (keV)	$E_{m,2}$ (10^{-3} cm^{-6} pc)	χ^2_ν	Mg[b]	Si[b]	Fe[b]
RS/solar	0.094	2.93	0.156	17.6	4.01	1.0	1.0	1.0
RS/MgSiFe.....	0.089	3.78	0.189	12.1	3.97	...	0.63	...
RS/variable.....	0.103	3.40	0.203	10.1	2.98	2.8	0.27	0.72
MEKAL/solar	0.112	3.51	0.231	9.11	3.75	1.0	1.0	1.0
MEKAL/MgSiFe.....	0.118	8.59	0.366	4.02	3.08	...	0.29	...
MEKAL/variable.....	0.115	9.10	0.332	4.56	2.71	0.24	0.13	0.34

[a] Equilibrium plasma emission models (see text).
[b] Elemental abundances relative to solar (Anders & Grevesse 1989).

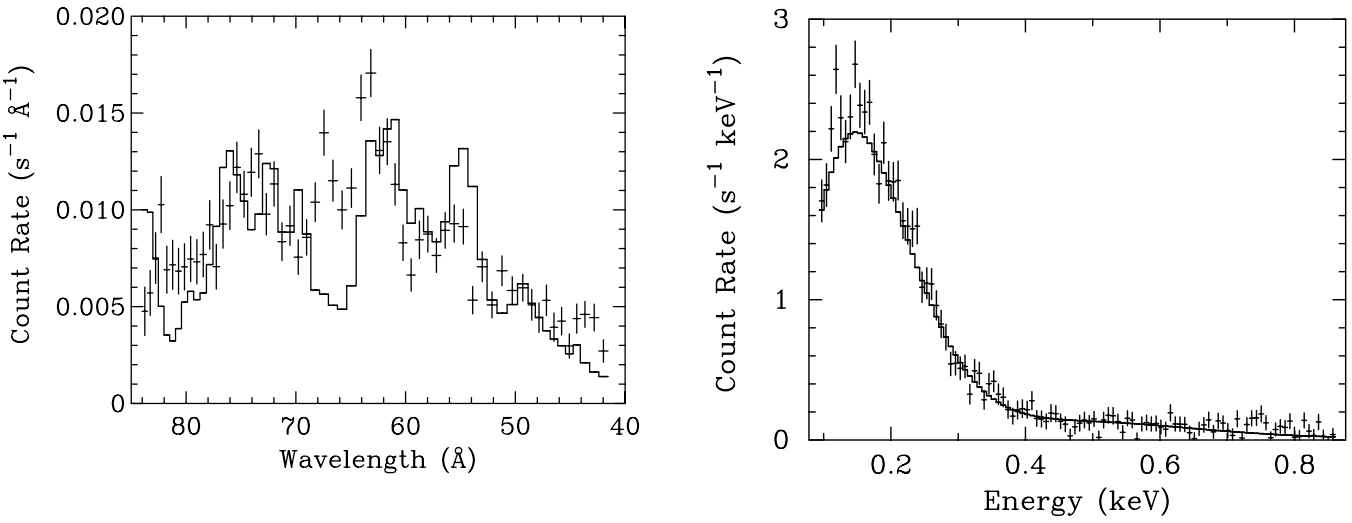

FIG. 13.—DXS HISM dispersed spectrum (*left*) and pulse-height spectrum (*right*) fitted by the solar abundance RS model described by eq. (1). Non–X-ray background has been subtracted from each spectrum.

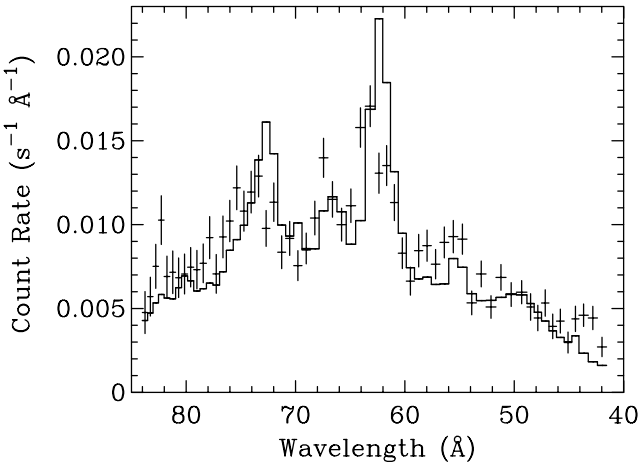

FIG. 14.—DXS HISM spectrum fitted by the variable abundance MEKAL model described by eq. (1) with individually adjustable abundances for Mg, Si, and Fe. The pulse-height spectral fit is similar to that of Fig. 13.

Since collisional equilibrium thermal plasma models fail to account for the HISM spectrum, we proceed to consider other types of models and comparisons.

4.3. *Nonequilibrium Plasma Models*

Section 4.1 indicates that the DXS HISM spectrum shows strong emission lines. Section 4.2 shows that current single-temperature collisional equilibrium plasma models do not fit the DXS data well, even if elemental abundances are allowed to vary. In principle, nonequilibrium ionization (NEI) model spectra can be quite different from equilibrium ones, as a different set of spectral lines are produced owing to the presence of ions different from those common in equilibrium at a given temperature and to a different balance between the collisional and recombination processes that populate excited states. Such models allow for greater variety at the expense of additional parameters. However, we find similar results from both equilibrium and NEI models with temperatures $\sim 10^6$ K: if they meet the constraints from the broadband fluxes (especially in the $\frac{3}{4}$ keV band), they cannot fit the DXS spectrum. This section presents the fits of a particular set of nonequilibrium models to the DXS data.

The picture of the diffuse X-ray background discussed in § 1 supposes that the Sun is inside a cavity that has been formed by one or more supernova explosions. Each supernova explosion shock heats the ambient gas in the interstellar medium and enlarges the boundary of the bubble. The equilibration time for the kinetic temperature in the gas is short compared to the ionization time, so the ionization state of the gas lags the kinetic temperature, and the gas is underionized. Edgar & Cox (1993) model the details of X-ray production in the single supernova explosion case and find that it is difficult to match even broadband observational parameters. Smith (1996) and Smith & Cox (2001), hereafter SC01, have modeled emission from multiple older co-located supernova explosions. The supernova explosions are separated by $1–2 \times 10^6$ yr and the current epoch is $4–8 \times 10^6$ yr after the first explosion. As the gas expands, and cools both adiabatically and by thermal conduction, it becomes overionized and then approaches equilibrium. The models include thermal conduction in the gas, the effects of dust cooling and sputtering, and the possibility of spatially varying abundances. SC01 find that models consisting of two or three supernova explosions fit the Wisconsin all-sky survey B and C band rates (McCammon et al. 1983) and other observational parameters reasonably well. However, comparison with the DXS HISM spectrum produces $\chi^2_\nu \gtrsim 7.9$.

The appearance and goodness-of-fit of the SC01 models are similar to those of the equilibrium solar-abundance RS model shown in Figure 13, particularly in the lack of emission at $64 \lesssim \lambda \lesssim 68$ Å. This is because the atomic physics calculations used in the SC01 models are the same as those used in RS. Also, several million years after the last explosion, the gas in the SC01 model is near equilibrium.

Thus, it is possible that the poor fit of the SC01 models to the DXS data is due to inadequate atomic physics data and models used to generate the X-ray spectra and not to any intrinsic shortfalls in the SC01 astrophysical model. Because the DXS calibration data fit the instrument model with good accuracy, we attribute the lack of a good fit by both equilibrium and nonequilibrium models to the astrophysics or to the atomic physics data, and not to the DXS instrument model.

4.4. *The Atomic Data and Models*

Since we are unable to fit straightforward models from the existing plasma emission model codes to the DXS HISM spectrum, we proceed to examine the contents of the models. We do this for two reasons: an attempt to identify features in the spectrum, and an attempt to derive a synthetic spectrum that is consistent with the data (and that perhaps will suggest new types of astrophysical models).

Current models of emission spectra from coronal plasmas such as the RS model and those of Mewe, Gronenschild, & van den Oord (1985); Mewe, Lemen, & van den Oord (1986), Kaastra (1992); and MEKAL indicate that the expected lines in the $\frac{1}{4}$ keV band are predominantly of two categories. The first category consists of L-shell lines of elements from neon to argon. These lines are the analogs of the Fe L-shell lines in the 0.7–1.2 keV energy band, i.e., $n = 3 \rightarrow 2$, $n = 4 \rightarrow 2$, and higher transitions. The second category of expected lines are M-shell lines of Fe ions and the ions of other iron-group elements.

To see which ions contribute lines in what parts of the spectrum, we extracted from the RS and MEKAL codes model spectra of single ions of the elements Ne, Mg, Si, S, Ar, Ca, Fe, and Ni that have lines in the DXS band. In many cases, the line ratios within the 84–44 Å band are not very temperature sensitive (although the absolute emissivity is). If these theoretical spectra are representative of coronal spectra from nature, they represent a set of approximate basis functions from which astrophysical spectra must be built. That is, a model with minimal astrophysical prejudice can be constructed from a linear combination of these spectral basis functions. Tradeoffs between various ions with nearly coincident lines can then be assessed, and astrophysical conclusions can be drawn from the relative normalization factors for the spectra of the ions of each element.

As an example of what is learned by comparing these spectra to the DXS data, we discuss the attempt to identify the strong emission feature that appears at 67.4 Å in the DXS HISM spectrum. The MEKAL spectrum of Ne VIII has one very strong line blend in the DXS band, which

occurs at 67.4 Å, plus a few weaker lines. To explore the conjecture that the 67.4 Å feature in the HISM spectrum might be produced by this Ne VIII line, we also looked at the RS spectrum of Ne VIII, and found that there the strongest line falls at 70 Å, and that there are also lines with a large fraction of the intensity of the 67.4 Å line at 61 Å and at 74 Å. To try to resolve these differences, new computations were obtained of the spectrum of Ne VIII (and a few other ions) at temperatures near 10^6 K from D. A. Liedahl (1996, private communication), who used the HULLAC code (Klapisch 1971). The RS and MEKAL models of Ne VIII each have four lines in the 84–44 Å band, the compilation of Kelly (1987) lists 23 lines, and Liedahl finds that 13 of the 17 lines included in his calculation contribute significantly in the DXS band. The Liedahl calculation shows a strong blend of lines ($4p \rightarrow 2s$ transitions) at the proper wavelength to match our 67.4 Å feature, but it also shows, twice as strong, a line blend near 74 Å ($4d \rightarrow 2p$ and $4s \rightarrow 2p$ transitions). The ratio of these lines is not very sensitive to the temperature. If these computations are accurate, it is highly unlikely that Ne VIII is the source of the 67.4 Å feature in the DXS HISM spectrum, since a stronger line blend around 74 Å should be present, but is not observed.

Liedahl (1999) suggests that the Fe IX $5d \rightarrow 3p$ transitions also occur very close to this wavelength, and should be considered. However, there are much stronger Fe IX lines ($4d \rightarrow 3p$ transitions) elsewhere in the band, near 82.5 and 83.5 Å in the Liedahl/HULLAC model. Unless the wavelengths of these lines are in error by several Å and are beyond the soft end of the DXS band, or their intensity relative to that of the 67.4 Å line is in error by more than a factor of 5, Fe IX cannot be responsible for a significant fraction of this spectral feature.

Similar considerations have ruled out a great many other possible line identifications, with candidates being taken from Kelly (1987). The solar spectra of Acton et al. (1985) and Malinovsky & Heroux (1973) both have features near this wavelength (see § 4.5). Acton et al. (1985) identify the feature as a blend of Ne VIII λ67.38 and Mg IX λ67.24, while Malinovsky & Heroux (1973) give Fe XVI $\lambda\lambda$66.2, 66.3 for their slightly shorter wavelength feature. The Mg IX candidate is ruled out because stronger lines from the same ion at 73.0 Å are not seen in the DXS spectrum. The presence of Fe XVI in general implies the existence of large amounts of Fe XVII, whose strong lines in the $\frac{3}{4}$ keV band are several times brighter than the total flux detected in this direction by the Wisconsin, *HEAO 1*, or *ROSAT* all-sky surveys. The 67.4 Å feature remains unidentified at this time.

Given the wide variation between different computations of the spectra of the same ions under the same conditions for most of the ions that have strong lines in this band, it appears that new, more accurate, calculations of the spectra of relevant ions are needed to make sense of the 84–44 Å band spectra of the diffuse X-ray background (or any other astrophysical source). This effort will be aided by the *Chandra X-Ray Observatory* Emission Line Project, which has taken deep grating spectra of relatively well-understood bright stars in an attempt to benchmark the astrophysical plasma emission codes. In a subsequent paper (Edgar et al. 2001, in preparation), we will use new calculations by Liedahl of the spectra of these ions to make astrophysical inferences about the DXS spectra.

Similar discrepancies between the models and astrophysical and laboratory spectra have been noted before, especially in the $\frac{3}{4}$ keV band. For example *EUVE* spectra of *Capella* allow one to model the distribution of emission measure *vs.* temperature (Brickhouse et al. 2000). Using this emission measure distribution and existing spectral models to synthesize a model X-ray spectrum for comparison with the simultaneous *ASCA* observation, it is clear that the accuracy and completeness of the Fe L-shell lines in the existing plasma X-ray emission codes (RS or MEKAL) is not adequate for interpreting modest resolution X-ray spectra ($E/\Delta E \lesssim 30$), as obtained for example with CCDs having resolution in the $\frac{3}{4}$ keV energy band similar to that of DXS in the 84–44 Å band. Many weak lines resulting from transitions up to $n = 7 \rightarrow 2$ must be included to obtain an adequate fit. The situation is being improved for the Fe L-shell lines (Liedahl et al. 1995), but similar work needs to be done on the lines of Ne, Mg, Si, S, and Ar in order to interpret spectra of astrophysical objects in the $\frac{1}{4}$ keV band. The discrepancies in the Fe L-shell lines are also observed under laboratory conditions. Liedahl (1999) points out differences between existing predictions and measurements made with the Electron Beam Ion Trap (EBIT) at Lawrence Livermore National Laboratory.

Not only are the currently available atomic data inadequate, but in many instances the treatment of the data within the existing plasma X-ray emission codes is also not adequate. The existing models were designed with lower energy resolution in mind, in part to accommodate the limitations of the computers available at the time the codes were conceived. For example, in many cases a multiplet of lines was grouped into a single "line," in the RS code as well as in the MEKAL code, in an effort to get the right flux at about the right energy, an approach that was entirely adequate for instruments with proportional counter resolution ($E/\Delta E \lesssim 5$).

4.5. *Comparison to Solar X-Ray Spectra*

We have compared the measured DXS spectra to solar spectra in the same wave band with similar or higher spectral resolution to see if the line identifications of the solar spectra could help with those of the DXS spectrum, as was attempted for the 67.4 Å feature discussed in § 4.4. Figure 15 presents three spectra of the solar corona, a plasma with $T \sim 10^6$ K, folded through the DXS response, and plotted along with the DXS HISM spectrum. The solar spectra are normalized such that the strength of the strongest line in the spectrum is similar to that of the strongest line of the DXS spectrum. The spectra of Malinovsky & Heroux (1973) and Acton et al. (1985) have only partial spectral coverage, $\lambda > 60$ Å and $\lambda \lesssim 80$ Å, respectively. The differences among the solar spectra may be explained by the fact that the Sun is not a quiescent object. The Malinovsky & Heroux (1973) spectrum is of the full disk, while that of Acton et al. (1985) is of a solar flare. The Doschek & Cowan (1984) spectrum is a composite line list, drawn from many measurements and theoretical calculations. It seems clear from these figures that the solar spectra are not that similar to the DXS spectra, which is not very surprising since the physical conditions in the hot interstellar medium are rather different from those in the Sun. As a result, the solar spectra were not helpful in the identification of features in the DXS spectrum.

4.6. *Fit to Multiple δ-Functions*

Since no straightforward astrophysical models computed with existing plasma emission codes can be made to fit the

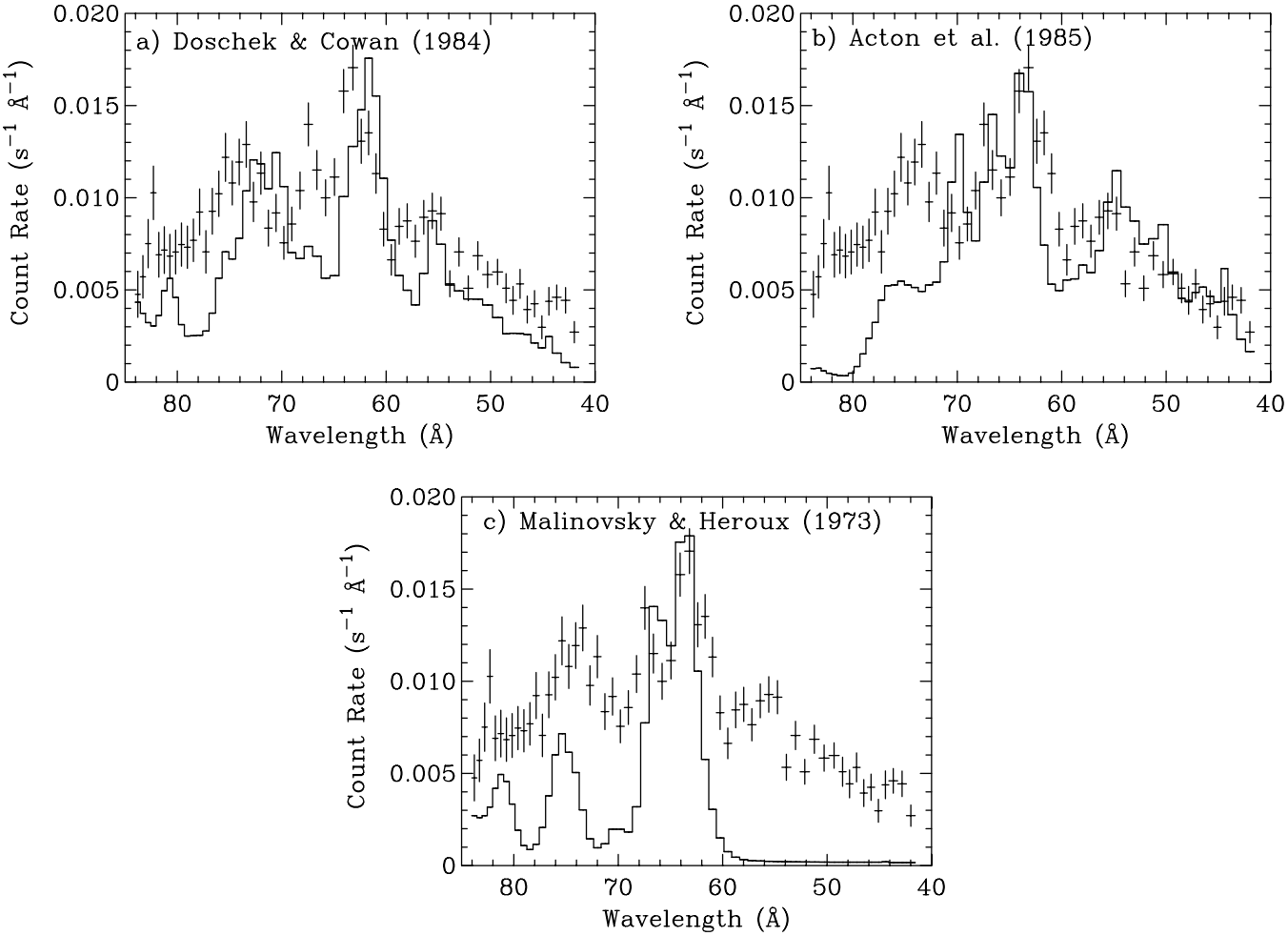

FIG. 15.—DXS HISM region spectrum (*data points*) compared to solar spectra (*solid lines*) of (*a*) Doschek & Cowan (1984), (*b*) Acton et al. (1985), and (*c*) Malinovsky & Heroux (1973).

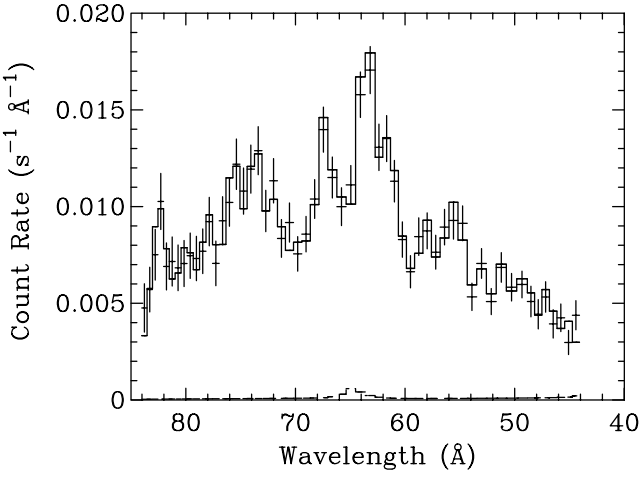

FIG. 16.—DXS HISM spectrum fitted with δ functions. The DXS pulse-height distribution and the Wisconsin sky survey broadband count rates were fit simultaneously. There are 23 δ-function lines in the 84–44 Å band with energies chosen by eye, two δ-function lines in the $\frac{3}{4}$ keV band with best-fit energies, and an absorbed power law component. The contribution of the $\frac{3}{4}$ keV δ-function lines and the power law to the 84–42 Å band is shown by the dashed line at the bottom.

DXS HISM spectrum, we have fitted it with an artificial spectrum consisting of a number of narrow spectral lines of selected wavelengths. Lines were added to the model one at a time, at the wavelength where the residual between the data and the model was greatest, until the reduced χ^2 fell below 1. The model was fitted simultaneously to the position and pulse-height spectra from the DXS HISM region and to the Wisconsin sky survey broadband data from the same region of the sky. By this procedure we demonstrate that it is possible to fit this data set with this response matrix and obtain a formally acceptable χ^2. It also provides a mechanism for determining the intensities of the lines or line blends of the DXS spectrum.

In addition to 23 δ-function components in the 84–42 Å DXS first-order band, we included two δ-function components in the $\frac{3}{4}$ keV band with freely floating energies, and the same absorbed power-law component, $e^{-\sigma N_{\rm H}} 11 E^{-1.4}$, as in the thermal models discussed above (§ 4.2). These last three components supply the necessary flux in the higher energy 0.44–6 keV bands of the Wisconsin sky survey, but they provide less than 1.5% of the total flux in the DXS 84–42 Å band and less than 7% of the flux in any bin in the

TABLE 3

LINE STRENGTHS[a]

E (eV)	λ (Å)	Intensity[b,c]
150.5.....	82.39	2.42 ± 0.22
153.1.....	80.99	0.42 ± 0.19
155.3.....	79.84	1.25 ± 0.17
159.3.....	77.83	1.48 ± 0.16
164.0.....	75.60	1.88 ± 0.16
168.5.....	73.58	1.89 ± 0.15
172.8.....	71.75	1.27 ± 0.13
176.8.....	70.13	0.72 ± 0.12
179.3.....	69.15	0.44 ± 0.11
183.0.....	67.75	0.55 ± 0.13
184.0.....	67.39	1.45 ± 0.14
188.4.....	65.81	0.84 ± 0.13
195.0.....	63.58	2.75 ± 0.15
202.0.....	61.38	1.50 ± 0.13
206.6.....	60.01	0.32 ± 0.11
213.4.....	58.10	1.17 ± 0.12
220.5.....	56.23	0.63 ± 0.12
224.2.....	55.30	1.10 ± 0.12
233.9.....	53.01	0.76 ± 0.11
243.0.....	51.02	1.02 ± 0.12
253.0.....	49.01	1.14 ± 0.16
264.0.....	46.97	1.02 ± 0.17
275.0.....	45.09	0.77 ± 0.18
569.0.....	21.79	13.46[d]
842.7.....	14.71	6.00[d]

[a] From the multiple δ-function fit to the HISM spectrum.

[b] Photon s^{-1} cm^{-2} sr^{-1}.

[c] 68.3% (1 σ) confidence limits.

[d] See text.

DXS position spectrum. The resulting model fits the DXS HISM position spectrum with a $\chi^2_\nu = 0.77$ for $\nu = 33$ dof. We then obtained 1 σ confidence limits for the intensity parameters in this model, using the "error" command of "xspec" version 10.0 with one parameter at a time free to vary. This follows the prescription of Lampton, Margon, & Bowyer (1976), investigating how the fit statistic varies as each line intensity parameter is varied in turn (holding the rest fixed). We take as 68.3% confidence limits those parameter values at which $\chi^2 = \chi^2_{\min} + 1.00$.

In Table 3, we list the energies, wavelengths, intensities, and 1 σ confidence limits of the 23 lines in the 84–42 Å band. For completeness, we also include the two lines in the $\frac{3}{4}$ keV band, but without confidence limits. These two lines are present in the model only to provide X-ray flux in the 0.5–1 keV band. The solid line of Figure 16 shows the spectral fit in the 84–42 Å first-order band, and the dashed line shows the contribution of the higher energy photons to the spectrum. This is the contribution in second and third orders of the two high-energy δ-function components and the absorbed power-law continuum component. When this spectrum is used to calculate *ROSAT* count rates, the $\frac{1}{4}$ keV band rate is 3% lower than the observed rate, the $\frac{3}{4}$ keV band rate is $\sim$ 20% higher than the observed rate, and the 1.5 keV band rate is $\sim$ 7% lower than the observed rate.

The energies of these lines in the 84–42 Å band are somewhat arbitrary, and the spectrum of the diffuse soft X-ray background is certainly more complex than this simple model of 23 narrow emission lines, but this spectrum is the best description we have currently for the low Galactic latitude spectrum of the X-ray background in the 84–42 Å band.

5. CONCLUSIONS

We have presented spectra of the diffuse X-ray background in the 84–44 Å (148–284 eV) range, with spectral resolution $\lesssim$2.2 Å (4 eV at 148 eV to 14 eV at 284 eV). The spectra show strong emission lines, implying a thermal origin for a significant fraction, if not all, of the diffuse background in the 84–44 Å (148–284 eV) range. As a very conservative absolute lower limit, lines contribute at least 32% of the measured flux. We also observed the Vela and Monogem Ring supernova remnants. The Monogem spectrum is similar in shape to the general diffuse X-ray background spectrum, but the Vela spectrum is noticeably different.

We find that the measured spectra are entirely consistent with previous broadband measurements of the same part of the sky by the Wisconsin sounding rocket survey, *SAS 3*, *HEAO 1*, and *ROSAT*.

We find that the existing atomic emission data for this energy band are not adequate to fit the measured spectrum of the hot interstellar medium. We will continue to work with atomic physicists to calculate new theoretical spectra of relevant ions, and to benchmark these spectra against astrophysical spectra of bright, relatively well-understood stars that have been obtained with the *Chandra X-ray Observatory*. When we have adequate atomic data for the lines of important ions at temperatures of order 10^6 K, we can proceed to answer questions such as whether the gas is in coronal equilibrium, and if not, what kind of nonequilibrium ionization is required to fit the spectra, and whether the elemental abundances are solar or depleted. The young, hot Vela supernova remnant is likely to exhibit nonequilibrium ionization. However, it remains to be seen whether this is also true of the older Monogem Ring remnant or the diffuse background. When good single-ion spectra are available, we can set upper limits to the emission measure of each ion $E_{m,\mathrm{ion}} = \int n_{\mathrm{ion}} n_e \, dl$ by requiring that the theoretical spectrum for each ion not exceed our observed spectrum at any wavelength. These constraints can then be compared with detections or upper limits of other instruments in other wavelength bands, and with models.

It is with great pleasure that we acknowledge much work contributed by the Space Flight Hardware Group at the Space Science and Engineering Center of the University of Wisconsin, Madison, especially Robert Paulos, Fred Best, Gene Buchholtz, Dean Dionesotes, Nikola Ciganovich, Michael Dean, Timothy Dirkx, Robert Herbsleb, William Hibbard, W. Warren Miller, Scott Mindock, Mark Mulligan, Brian Paul, Dave Petre, Evan Richards, Jerry Sitzman, John Short, Mark Werner, and W. Walter Wolf.

We thank Kurt Jaehnig, who built the flight proportional counters, and several generations of other scientists, postdocs, graduate students, and undergraduate students in the Space Physics Laboratory of the University of Wisconsin, Madison, especially Jeff Bloch, Richard J. Borken, David N. Burrows, Jiahong Zhang Juda, Mike Juda, Julie Mills, Anisong Pathamavong, Mark Skinner, and Steve Snowden. We are pleased to acknowledge help with quick-look data analysis from Keith Jahoda, Rich Kelley, Alan Smale, Carolyn Stahle, and Andy Szymkowiak of the Goddard Space Flight Center Laboratory for High-Energy Astro-

physics, and we thank Duane Liedahl for providing his atomic physics calculations in advance of publication. We thank the referee, Steve Snowden, for the many helpful suggestions arising from his thorough reading of the manuscript. This work has been supported under NASA contract NAS 5-26078 and grants NAG 5-3080, NAG 5-3524, and NAG 5-629 to the University of Wisconsin, Madison. R. J. E. acknowledges support from NASA contracts NAS 8-40224 and NAS 8-39073 with the Smithsonian Astrophysical Observatory.

REFERENCES

Acton, L. W., Bruner, M. E., Brown, W. A., Fawcett, B. C., Schweizer, W., & Speer, R. J. 1985, ApJ, 291, 865
Anders, E., & Grevesse, N. 1989, Geochim. Cosmochim. Acta, 53, 197
Arnaud, K. 1996, in ASP Conf. Ser. 101, Astronomical Data Analysis Software and Systems V, ed. G. Jacoby & J. Barnes (San Francisco: ASP), 17
Bastin, G. F., & Heijligers, H. J. M. 1992, Microbeam Anal., 1, 61
Bloch, J. J. 1988, Ph.D. thesis, Univ. Wisconsin, Madison
Bloch, J. J., Jahoda, K., Juda, M., McCammon, D., Sanders, W. T., & Snowden, S. L. 1986, ApJ, 308, L59
Bloch, J. J., Priedhorsky, W. C., & Smith, B. W. 1990, in IAU Colloq. 115, High-Resolution X-ray Spectroscopy of Cosmic Plasmas, ed. P. Gorenstein & M. Zombeck (Cambridge, UK: Cambridge Univ. Press), 160
Borken, R. J., & Kraushaar, W. L. 1976, Space Sci. Instrum., 2, 277
Bowyer, C. S., Field, G. B., & Mack, J. E. 1968, Nature, 217, 32
Breitschwerdt, D., & Schmutzler, T. 1994, Nature, 371, 774
Brickhouse, N. S., Dupree, A. K., Edgar, R. J., Liedahl, D. A., Drake, S. A., White, N. E., & Singh, K. P. 2000, ApJ, 530, 387
Bunner, A. N., Coleman, P. L., Kraushaar, W. L., McCammon, D., Palmieri, T. M., Shilepsky, A., & Ulmer, M. 1969, Nature, 223, 1222
Burrows, D. N. 1982, Ph.D. thesis, Univ. Wisconsin, Madison
Burrows, D. N., & Mendenhall, J. A. 1991, Nature, 351, 629
Burstein, P., Borken, R. J., Kraushaar, W. L., & Sanders, W. T. 1977, ApJ, 213, 405
Cox, D. P., & Reynolds, R. J. 1987, ARA&A, 25, 303
Cox, D. P., & Smith, B. W. 1974, ApJ, 189, L105
Doschek, G. A., & Cowan, R. D. 1984, ApJS, 56, 67
Dwek, E. 1987, ApJ, 322, 817
Edgar, R. J., & Cox, D. P. 1993, ApJ, 413, 190
Edwards, B. C. 1990, Ph.D. thesis, Univ. Wisconsin, Madison
Garmire, G., Nousek, J. A., Apparao, K. M. V., Burrows, D. N., Fink, R. L., & Kraft, R. P. 1992, ApJ, 399, 694
Henke, B. L., Lee, P., Tanaka, T. J., Shimabukuro, R. L., & Fujikawa, B. K. 1982, At. Data Nucl. Data Tables, 27, 1
Henry, R. C., Fritz, G., Meekins, J. F., Friedman, H., & Byram, E. T. 1968, ApJ, 153, 11
Holliday, J. E. 1967, The Norelco Reporter, XIV, 84
Jahoda, K., & McCammon, D. 1988, Nucl. Instrum. Methods Phys. Res., A272, 800
Jelinsky, P., Vallerga, J. V., & Edelstein, J. 1995, ApJ, 442, 653
Juda, M., Bloch, J. J., Edwards, B. C., McCammon, D., Sanders, W. T., Snowden, S. L., & Zhang, J. 1991, ApJ, 367, 182
Kaastra, J. 1992, An X-Ray Spectral Code for Optically Thin Plasmas (Internal SRON-Leiden Rep., updated version 2.0)
Kelly, R. L. 1987, J. Phys. Chem. Ref. Data, 16, 1
Klapisch, M. 1971, Comput. Phys. Commun., 2, 239
Kuntz, K. D., & Snowden, S. L. 2000, ApJ, 543, 195
Lampton, M., Margon, B., & Bowyer, S. 1976, ApJ, 208, 177
Liedahl, D. 1999, Phys. Scr., T83, 110
Liedahl, D. A., Osterheld, A. L., & Goldstein, W. H. 1995, ApJ, 438, L115
Malinovsky, L., & Heroux, M. 1973, ApJ, 181, 1009
Marshall, F. J., & Clark, G. W. 1984, ApJ, 287, 633
McCammon, D., Burrows, D. N., Sanders, W. T., & Kraushaar, W. L. 1983, ApJ, 269, 107
Mewe, R., Gronenschild, E. H. B. M., & van den Oord, G. H. J. 1985, A&AS, 62, 197
Mewe, R., Kaastra, J. S., & Liedahl, D. A. 1995, Legacy, 6, 16
Mewe, R., Lemen, J. R., & van den Oord, G. H. J. 1986, A&AS, 65, 511
Morgenthaler, J. P. 1998, Ph.D. thesis, Univ. Wisconsin, Madison
Morrison, R., & McCammon, D. 1983, ApJ, 270, 119
Raymond, J. C., & Smith, B. W. 1977, ApJS, 35, 419
Sanders, W. T., et al. 1992, Proc. SPIE, 1743, 60
———. 1993, Proc. SPIE, 2006, 221
Sfeir, D. M., Lallement, R., Crifo, F., & Welsh, B. Y. 1999, A&A, 346, 785
Skinner, H. W. B. 1940, Proc. R. Soc. London A, 239, 95
Smith, R. K. 1996, Ph.D. thesis, Univ. Wisconsin, Madison
Smith, R. K., & Cox, D. P. 2001, ApJS, in press
Smith, R. K., Krzewina, L. G., Cox, D. P., Edgar, R. J., & Miller, W. W. 1996, ApJ, 473, 864
Snowden, S. L. 2001, in The Century of Space Science, ed. J. Bleeker, J. Geiss, & M. Huber (Dordrecht: Kluwer), in press
Snowden, S. L., Cox, D. P., McCammon, D., & Sanders, W. T. 1990, ApJ, 354, 211
Snowden, S. L., Egger, R., Finkbeiner, D. P., Freyberg, M. J., & Plucinsky, P. P. 1998, ApJ, 493, 715
Snowden, S. L., Mebold, U., Hirth, W., Herbstmeier, U., & Schmitt, J. H. M. M. 1991, Science, 252, 1529
Snowden, S. L., et al. 1997, ApJ, 485, 125
———. 1995, ApJ, 454, 643
Welsh, B. Y., Crifo, F., & Lallement, R. 1998, A&A, 333, 101
Welsh, B. Y., Sfeir, D. M., Sirk, M. M., & Lallement, R. 1999, A&A, 352, 308
Williamson, F. O., Sanders, W. T., Kraushaar, W. L., McCammon, D., Borken, R., & Bunner, A. 1974, ApJ, 193, L133